Discrete Element Method and Electrochemical Modelling of Lithium Ion Cathode Structures Characterised by X-ray Computed Tomography

*Ruihuan Ge[1,4], Adam M. Boyce[2,4], Ye Shui Zhang[2,3,4], Paul R. Shearing[2,4], Denis J. Cumming[1,4], Rachel M. Smith[1,4]**

[1]Department of Chemical and Biological Engineering, The University of Sheffield, Sheffield, S10 2TN, UK

[2]Electrochemical Innovation Lab, Department of Chemical Engineering, University College London, London, WC1E 7JE, UK

[3]School of Engineering, University of Aberdeen, Aberdeen, AB24 3UE, UK

[4]The Faraday Institution, Quad One, Harwell Science and Innovation Campus, Didcot, OX11 0RA, UK

** Corresponding author: rachel.smith@sheffield.ac.uk*

Abstract

Electrode microstructure can profoundly affect the performance of lithium-ion batteries. In this work, the effect of the calendering process on electrode microstructures is investigated using the Discrete Element Method (DEM) with a bonded particle model. A comprehensive evaluation between realistic electrode structures and idealised DEM structures as characterised using X-ray computed tomography (XCT) is presented. The electrode structural and transport properties of tomography scans and DEM structures, i.e. porosity distribution, specific surface area and tortuosity factors are studied. Following consideration of the carbon binder domain (CBD) phase, electrochemical analysis is further performed. Excellent agreement between tomography and idealised structures from DEM simulations is achieved, taking into account the effect of calendering. With electrode compression battery performance is improved after calendering. This study provides a basis for using DEM and electrochemical analysis to quantitatively evaluate the battery performance in future.

Key words: Discrete Element Method, Lithium-ion battery, Calendering, X-ray computed tomography, Electrochemical analysis

1. Introduction

Lithium-ion batteries play a critical role in the energy storage field. They can be widely used for electric vehicles and portable electronics due to the advantages of high capacity and high power. The rapid development of electric vehicles requires high energy density, high cycle life and low cost [1]. Challenges still remain to further improve the manufacturing procedures and electrode design. In particular, the porous electrode microstructures can affect the battery performance including mechanical and electrochemical properties [2].

XCT has been widely used to characterise the microstructural heterogeneities of electrodes, for example Ebner et al. [3] characterised the 3D microstructure of $LiNi_xMn_yCo_zO_2$ (NMC) based cathodes under different calendering pressures. A battery cathode structure contains three different phases, i.e. the active material (AM) particle phase, the CBD phase, and the pore space. In the work of Ebner et al., tomographic data including identified individual AM particle positions were obtained [3]. However resolving the details of the CBD phase usually needs high resolution techniques, e.g. nano-computed tomography, focused ion beam/scanning electron microscopy (FIB–SEM) [4]. By combining XCT and FIB-SEM, Zielke et al. [5] proposed a hierarchical reconstruction approach of electrode structures wherein the effect of nanoporosity within the CBD was considered. Daemi *et al.* [4] visualised the CBD phase using a combination of X-ray nano-computed tomography and FIB-SEM. A novel approach called dual-scan superimposition technique was developed by Lu *et al*. [6]. The features of NMC particles and nano-sized CBD phase can be captured and reconstructed by X-ray nano-computed tomography. The microstructure characterisation results show that the structure variations can significantly affect the transport properties and electrochemical performance of electrodes [5, 7].

During electrode manufacturing, the calendering process is a key step when tailoring the microstructure of electrodes. Previous research has shown that the calendering process affects battery performance in different ways [8, 9]. An optimal electrode porosity and corresponding calendering condition can be found to achieve the best performance for a given electrode, however this optimisation has historically been achieved empirically [10]. The AM particles within cathode structures usually have low electronic conductivity. The compression of the electrode structures can significantly affect the particle contacts and carbon network within electrodes, and improve electronic conductivity. A recent study reported the effect of calendering process on the electrochemical performance of high-nickel, cobalt-free cathode structures [11]. Under high calendering pressures (25 % and 35 % porosities), particle pulverisation and fusion can occur, however the electrochemical performance was improved without capacity and cycle life loss. Due to the importance of the calendering process, some novel numerical and experimental techniques have been performed. Duquesnoy et al. [12] proposed a data-driven assessment approach of electrode calendering processes. Electrode structures under different calendering pressures were generated virtually, and properties such as tortuosity and effective conductivity were further evaluated using machine learning. Lu et al. [13, 14] investigated the electrode structure evolution during calendering by an *in stu* calendering experiment and X-ray nano-computed tomography and subsequently performed microstructure optimisation.

The DEM can be used to model the motions and forces of individual particles within electrodes. Using DEM, detailed particle scale information including particle contacts, stress and porosity can be obtained and analysed [15, 16]. It has been used to investigate the electrode structure evolutions during calendering [17, 18]. In addition, it can be further applied to understand how the electrode microstructure evolution affects transport properties and electrochemical performance. Srivastava et al. [19] investigated the binder adhesion effect on the electrode mesostructrue and corresponding transport properties. In their work, stochastically generated structures were used in DEM. Their results showed that the cohesion and adhesion of CBD phases and AM particles play an important role in determining the battery performance. Another relevant work was proposed by Ngandjong et al. [20] to numerically study the electrode calendering process and the corresponding electrochemical performance. The previous research works demonstrate that DEM could be a promising way to investigate the performance/microstructure relationship in electrodes. Currently, most DEM work in this field is based on virtual particle structures, and lack experimentally generated micro-structural information for verification and validation. With improving XCT facilities, there are emerging opportunities in this field to benchmark the performance of DEM simulated electrode structures by comparing with realistic electrodes characterised by XCT, and to further address the applicability of DEM generated structures for electrochemical analysis.

In this work, lithium ion cathode structures were characterised by high resolution XCT. Detailed structural properties including AM particle sphericity and orientation were evaluated. The uncalendered AM particle structure is used as the initial structure for DEM simulations. A comprehensive comparison of DEM generated structure and corresponding structure from tomography scans has been made. Electrochemical analysis was further performed by considering different calendering levels and the CBD phase. The comparative results demonstrate the applicability of DEM simulations for modelling the evolution of realistic electrode structures. After calendering the battery shows improved performance particularly at 1C. It is demonstrated that combining high fidelity electrochemical simulations with DEM provides a promising coupled technique to quantitatively evaluate battery performance under different calendering and manufacturing conditions.

2. Methodology

2.1 Experiment and image processing

Electrode structures were formulated of 96 wt.% $LiNi_{0.6}Mn_{0.2}Co_{0.2}O_2$ (NMC622, BASF), 2 wt.% C_{65} carbon black (Imerys) and 2 wt.% PVDF (Solvay). All powders were dried at 120 °C in a vacuum oven over 12 h to remove moisture. Details of the procedure for making the electrode slurries have been reported previously [21]. A THINKY mixer (ARE-20, Intertronics) was used to mix the cathode binder solution (PVDF and N-methyl pyrrolidone, NMP) at 2000 rpm for 15 min until the solution became homogenous. Afterwards, NMC622 and C_{65} were added slowly to the binder solution. The generated slurry was then mixed again at 2000 rpm for two periods of 15 min, 5 min apart, to cool down the slurry. The homogenous slurry was degassed in the THINKY mixer at a speed of 2000 rpm for 2 min. The slurry was coated onto a piece

of aluminium foil with a thickness of ~16 μm (PI-KEM) using a doctor blade thin-film applicator, resulting in a wet electrode of ~280 μm thickness. The slurry cast coatings were subsequently dried on a pre-heated hotplate (Nickel-Electro Clifton HP1-2D) with digital control and an aluminium plate (457w x 305d mm) at 60 °C. The dried electrode was calendered twice using a rolling press with MTI MSK-HRP-MR100DC calendering equipment.

The cathode structures were characterised by XCT with a 337 nm resolution. In this work, one uncalendered structure and one calendered structure were used for comparison with the DEM predictions. A cross section of the raw tomography scan is shown in Figure 1 (a). The machine-learning-based image analysis tool, *Ilastik* [22] was used to predict the volume fraction of different phases, i.e. AM particle phase, CBD phase and macro-pore phase (Supplementary Figure 1). Detailed volume fractions of different phases are listed in Table I.

The raw tomography scans are firstly filtered and binarised to obtain the AM particle phase (Figure 1 b). After binarisation, a segmentation procedure is implemented to separate and label the individual AM particles [23] (Figure1 c), the volume and coordinates of each individual particle were obtained. The particles within the cathode structure are approximated as spherical particles in DEM simulations (Figure 1 d).

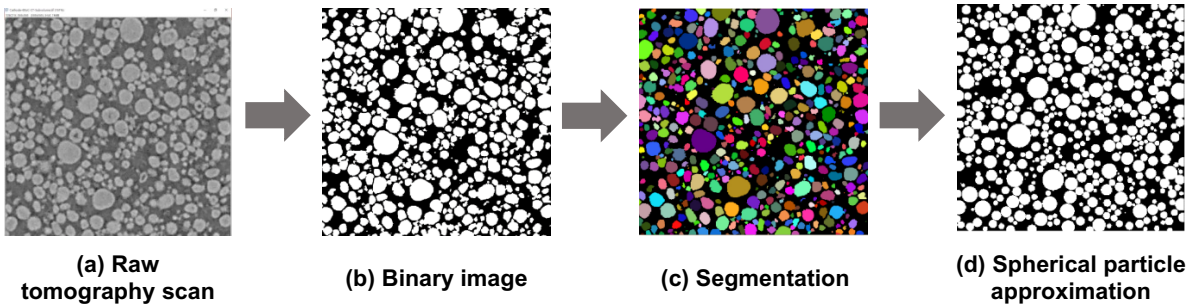

Figure 1 Image processing procedure of the AM particle phase.

Table I Volume fraction of electrodes studied.

Material	Structure	Volume fraction ε (%)		
		AM particle	CBD phase	Macro pore
NMC 622	Uncalendered structure	48.34	40.14	11.52
	Calendered structure	59.69	34.12	6.19

2.2 DEM simulation

In this work, DEM was applied to investigate the effect of the calendering process on the electrode structure evolution. In DEM, the motion and forces of an individual particle can be described by:

$$m\frac{d\boldsymbol{v}}{dt} = \boldsymbol{F}_{\mathrm{b}} + \boldsymbol{F}_{\mathrm{p}} \quad (1)$$

$$I\frac{d\boldsymbol{\omega}}{dt} = \boldsymbol{M}_{\mathrm{b}} + \boldsymbol{M}_{\mathrm{p}} \quad (2)$$

where m and I are the particle mass and moment of inertia. $\boldsymbol{v}$ and $\boldsymbol{\omega}$ are the translational velocity and angular velocity. $\boldsymbol{F}_{\mathrm{p}}$ and $\boldsymbol{M}_{\mathrm{p}}$ are the contact force and contact torque between neighbouring particles. In this work, a bond model is used to describe the CBD phase interactions (Figure 2 a). $\boldsymbol{F}_{\mathrm{b}}$ and $\boldsymbol{M}_{\mathrm{b}}$ are the bond force and bond torque. An Edinburgh elasto-plastic adhesive (EEPA) model and bonded particle model were used to describe the interactions of AM particles and CBD phase [24, 25]. Detailed mathematical equations and DEM simulation parameters are given in Supplementary Tables 1-4.

As illustrated in Figure 2 (b), the uncalendered electrode structure processed from tomography scans is imported into the Altair EDEM software, and inter-particle bonds were assigned to the electrode structure. The particle size distribution (PSD) calculated from equivalent spherical particles is compared with the PSD characterised experimentally using laser diffraction. As shown in Figure 2 (c), the good agreement between tomography and laser diffraction indicates the processed tomography data has represented the PSD accurately. The structure was compressed by moving the top plate with a constant speed of 0.01 m/s to mimic the calendering process. The top plate was made of steel to model the roller, and the bottom plate is aluminium to model the current collector. Periodic boundaries were applied during the simulation. During the DEM simulation, the electrode structure was compressed by moving the top plate down. As illustrated in Figure 2 (d), the porosity-pressure relationship was obtained from the DEM simulation. In this figure the porosity $\varepsilon_{\mathrm{Pore+binder}}$ is the interstitial void volume fraction including both the pore and binder phase between AM particles. In order to validate the DEM model, the simulation results are compared with the experimental data using a same 96 % AM particle mass loading and PSD [3]. The results show that the proposed model can capture the porosity evolution during calendering.

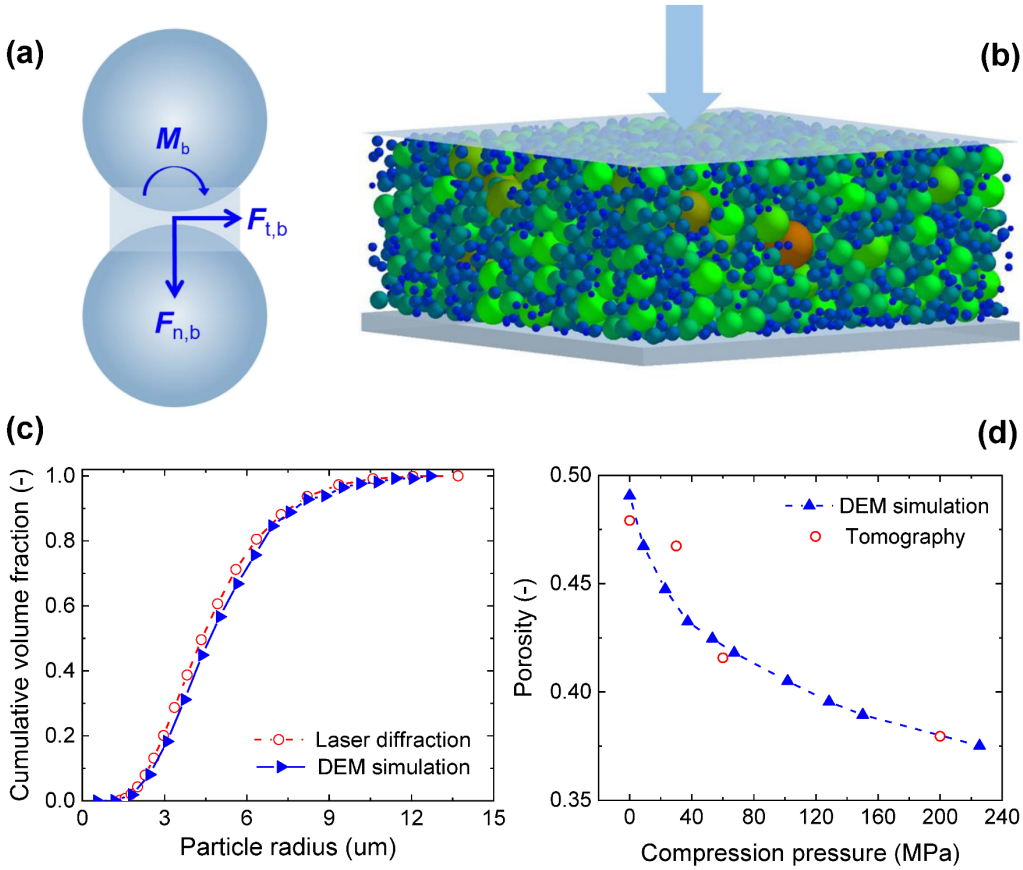

Figure 2 DEM simulation setup (a) Inter-particle bond (b) Compression test (c) AM particle size distribution (d) Porosity-pressure relationship from DEM simulation [3].

2.3 Microstructure analysis approach

The electrode microstructures before/after calendering were analysed by calculating porosity, specific surface area and tortuosity factors. These property variations can significantly affect the battery performance during calendering. In this work, a MATLAB application *TauFactor* was used to calculate specific surface area and tortuosity factors [26]. 3D voxelised images were used during the analysis. The specific surface area (SSA) is defined as the total surface area S_{Total} normalised by the total volume of the structure V_{Total}:

$$SSA = S_{\mathrm{Total}}/V_{\mathrm{Total}} \tag{3}$$

The tortuosity factor τ can be calculated by numerically solving steady diffusion equations which have the following relationship:

$$D^{\mathrm{eff}} = D\frac{\varepsilon}{\tau} \tag{4}$$

where D^{eff} is the diffusivity of the structure, D is the intrinsic diffusivity, and ε is porosity.

2.4 Electrochemical characterisation and simulation

2.4.1 Electrochemical characterisation

For making coin cells, the electrodes were cut into 15 mm discs. A Celgard separator was cut into 19 mm discs to avoid short circuits. All the coin cell components were dried overnight in a vacuum oven at 80 °C to remove any moisture before assembly. Seventy microlitres of electrolyte (1 mol L^{-1} lithium hexafluorophosphate in ethylene carbonate: dimethyl carbonate (1:1 vol%) with 2 wt% vinylene carbonate 99.9%) was used in each cell. After the assembly of the coin cells, a formation step composed of two CC-CV charge-discharge cycles at a C-rate of C/20 (C/50 cut-off) was conducted within a voltage window of 2.5 to 4.2 V vs Li/Li^+ for cathode half-cells, where the half cells contained a lithium metal counter electrode [21]. Electrochemical tests were carried out using a BCS-805 Biologic battery cycler (Biologic, France). The cells were then charged at a constant current C/10 and corresponding to discharged C-rates of C/10, C/5, C/3, and 1C.

2.4.2 Finite element implementation

Simpleware ScaniP was used to mesh the segmented volume images, giving approximately 10 million linear tetrahedral elements, with 5.2 million degrees of freedom. The theoretical framework, which is outlined in Supplementary Tables 5-8 was implemented in the finite element software COMSOL Multiphysics (v5.6, Sweden) using a 3D tomography based mesh as described. The Parallel Direct Sparse Solver (PARDISO) was used to solve the discretised transport and electrode kinetics equations. A segregated approach was taken which involved solving the coupled field variables in a sequential, staggered way. Time stepping was handled using 2^{nd} order backward Euler differentiation.

3. Results and discussion

3.1 AM particle structure analysis

The shape and orientation angles of individual AM particles from tomography scans were firstly analysed. The probability distributions of particle sphericity and orientation angle are presented in Figure 3. Sphericity defined by [27] is used to describe the particle shape. As shown in Figure 3 (a), the range of sphericity varies between 0.6 and 1.0. The probability distribution moves to the left after calendering, corresponding to a decreasing mean sphericity from 0.82 to 0.80. The particle orientation is defined as the angle between the longest axis of particle and z-axis perpendicular to the current collector. As shown in Figure 3 (b), the probability distribution shows an increasing trend from 0^o to 45^o, and it levels off afterwards. The corresponding mean orientation angles of the uncalendered and calendered structures are 52.5^o and 55.5^o, indicating the particles are orientated horizontally along the current collector. For the calendered structure, the slight decrease in particle sphericity and increase in particle orientation angle can be attributed to the occurrence of particle deformation and rotation during calendering. To address the effect of particle shape and orientation, an ellipsoid approximation is used to describe the particle packing from tomography scans.

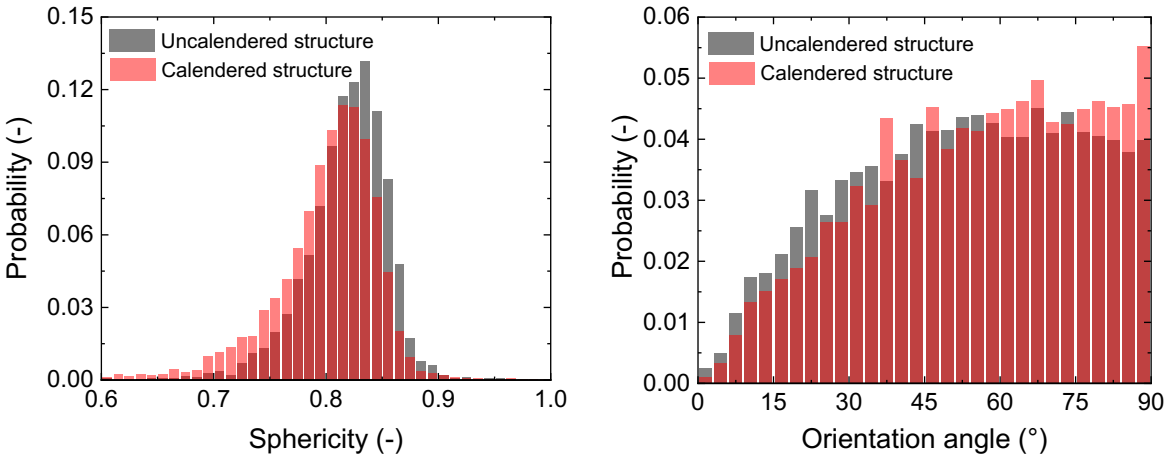

Figure 3 Probability distributions of sphericity and orientation angles of AM particles from tomography scans.

Figure 4 presents the porosity distribution of different structures. The experimental validation is based on the XCT structures. In general, MIP measurements for an electrode will provide the combined pore size distribution arising from both the microstructural arrangement of active particles and the porous CBD phase. The pores of each phase and their relative contributions to the overall pore size distribution, as obtained from MIP, cannot currently be decoupled to make a comparison with the particle structure from DEM. Two pore size distribution calculation approaches were considered for both XCT structures and virtual DEM structures, i.e. the continuous pore size distribution (c-PSD) and the mercury intrusion porosimetry pore size distribution (MIP-PSD) [28]. When using the c-PSD approach, the porous phase was filled with spheres with a certain radius *r*. The amount of pore volume that can be occupied by spheres with a certain radius *r* was calculated. This was repeated by gradually increasing the test sphere radius until a cumulative pore size distribution was calculated. The MIP approach models the process of mercury intrusion into porous structure, and average pore bottleneck size distribution was calculated. The c-PSD and MIP-PSD results for the DEM simulated structures, ellipsoid structures and corresponding tomography scans are presented in Figure 4. For all porosity distribution curves, they show three different stages: the initial stage of high cumulative pore volume fraction with nearly zero slope, afterwards the pore volume fraction drops rapidly, and finally it drops to zero with a relatively low slope. For both uncalendered structure and calendered structure, the MIP curve decreases more drastically than the corresponding c-PSD curve. As illustrated in Figure 4, the porosity distribution from DEM simulation and ellipsoid structure show similar variation tendency with the corresponding tomography scans for both calendered and uncalendered structures. The pore radius values corresponding to 50% cumulative pore volume fraction are calculated. The structures from tomography scans have the smallest pore radius for both c-PSD and MIP approach, and there is a slight increase after using spherical or ellipsoidal approximation. For the spherical particle structure in DEM simulations, the results show a less than 10 % increase of the pore size. This is the first time that such comparison of full pore size distribution is made in the literature. The results show that DEM simulations using spherical particle approximations can capture the porosity distribution evolution during calendering.

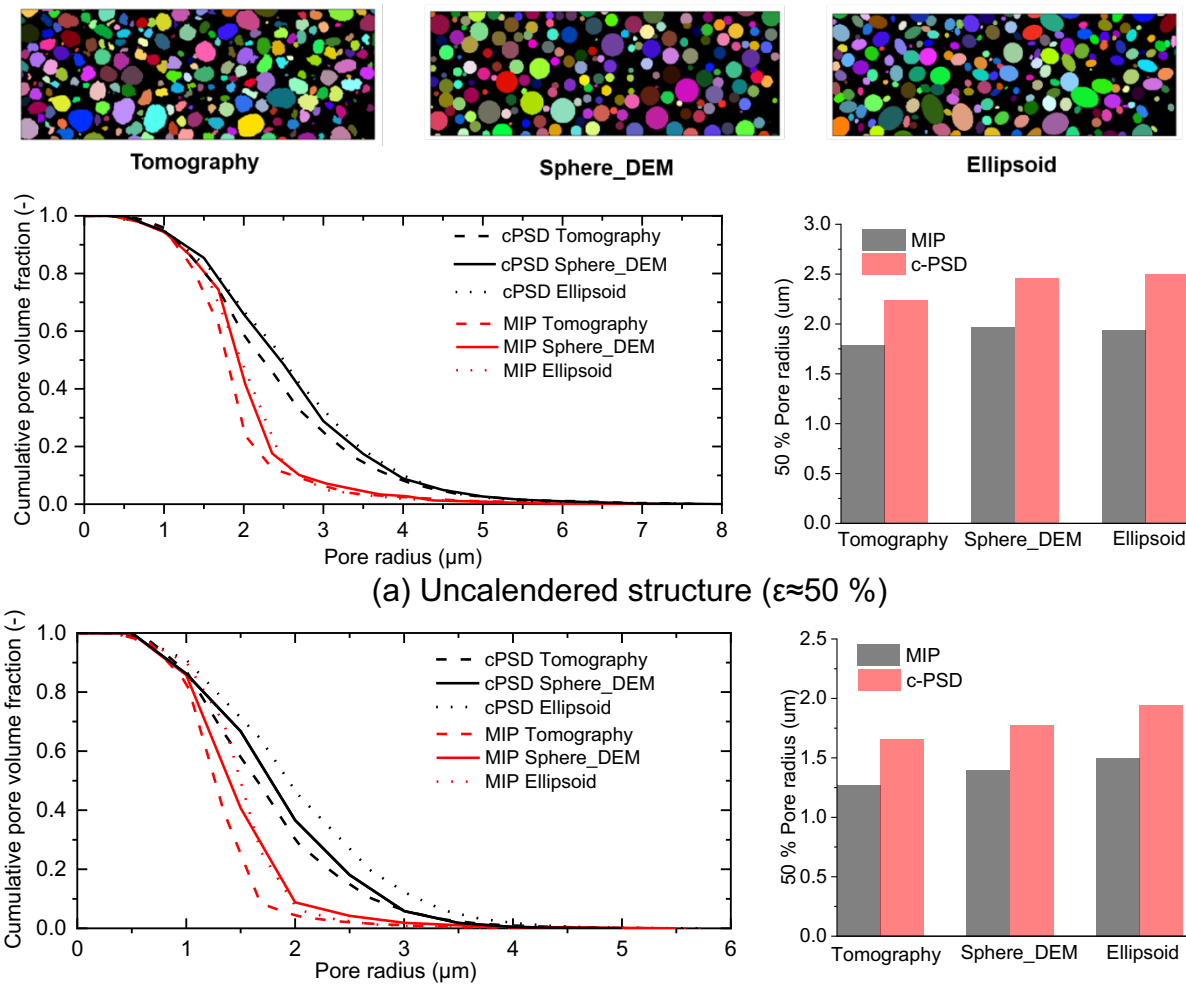

(a) Uncalendered structure (ε≈50 %)

(b) Calendered structure (ε≈40 %)

Figure 4 Porosity distribution and 50 % pore radius for both uncalendered and calendered structures based on c-PSD and MIP, electrode structures are from tomography scans, spherical approximations and ellipsoidal approximations.

The specific surface area and tortuosity values for both uncalendered and calendered structures under different conditions are calculated and presented in Figure 5. In this figure, the specific surface area and tortuosity account for the active particles. As expected, for all cases the specific surface area increases after calendaring (Figure 5 a). The values range from 0.44 to 0.6 μm^{-1} which is consistent with previous work [29]. Due to the spherical or ellipsoidal shape approximation, the specific surface area values of DEM simulated structures and ellipsoidal structures are slightly lower than the corresponding tomography structures. In Figure 5 (b), the tortuosity factors of DEM simulated structures and ellipsoid structures are compared with the structures from XCT under different conditions. For the average tortuosity factors, the value range of uncalendered structures is about 1.50-1.61, and it increases to about 1.68-1.86 after calendering. This result of structures from the tomography scan is about 5% to 10% higher than the corresponding DEM simulated structures and ellipsoid structures. The varied specific surface area and tortuosity are highly relevant to the battery performance. After calendering, the porosity of battery electrode decreases, with an increased "twistedness" of porous phase. The tortuosity value is higher than the

uncalendered structure, indicating that the effective diffusivity is decreased. By contrast, specific surface area increases as the particle packing becomes denser after calendering, enabling better Li+ ion diffusion properties at the interface.

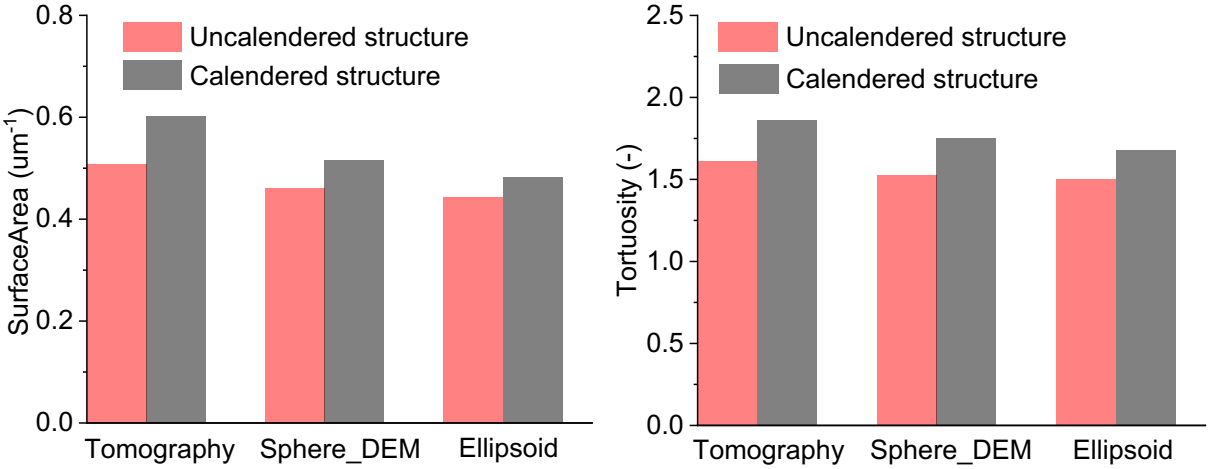

(a) Specific surface area (b) Average tortuosity

Figure 5 Specific surface area and tortuosity values for both uncalendered and calendered structures under different conditions.

The results from Figures 4-5 indicate that, the DEM simulation generated structures based on spherical particle approximation can capture the porosity distribution for both uncalendered and calendered structures. When considering the specific surface area and tortuosity factors, a slight discrepancy can be observed compared with the tomography scans. This is probably due to the spherical particle shape approximation in DEM. However, by using ellipsoidal particle structures considering particle orientations, the prediction results are not substantially improved. Therefore, in the following the DEM generated idealised structures using spherical particles under different calendering levels are further investigated and compared with the corresponding experimental results. Detailed microstructural evolution during DEM simulation is illustrated in Figure 6. The DEM generated AM particle structures were converted to 3D voxelised images. The 3D volumes have a cross-section size of 200 μm x 200 μm and the thickness values vary from ca. 49 μm to 71 μm. Figure 6 (a) shows the voxelised 3D structures and corresponding distance maps. The distance map is the calculated shortest path length along the through plane direction. Figure 6 (b) illustrates the inter-particle distance calculated by Euclidean distance transform. The results show the decreased inter-particle gap as a function of progressive calendering. Figure 6 (c) illustrates the normalised flow velocity field of the porous electrode structures by calculating the Navier-Strokes flow equations. The permeability decreases from 2.5×10^{-13} m^2 to 6.5×10^{-14} m^2, indicating the effect of calendering on the pore phase transport properties and microstructure heterogeneity.

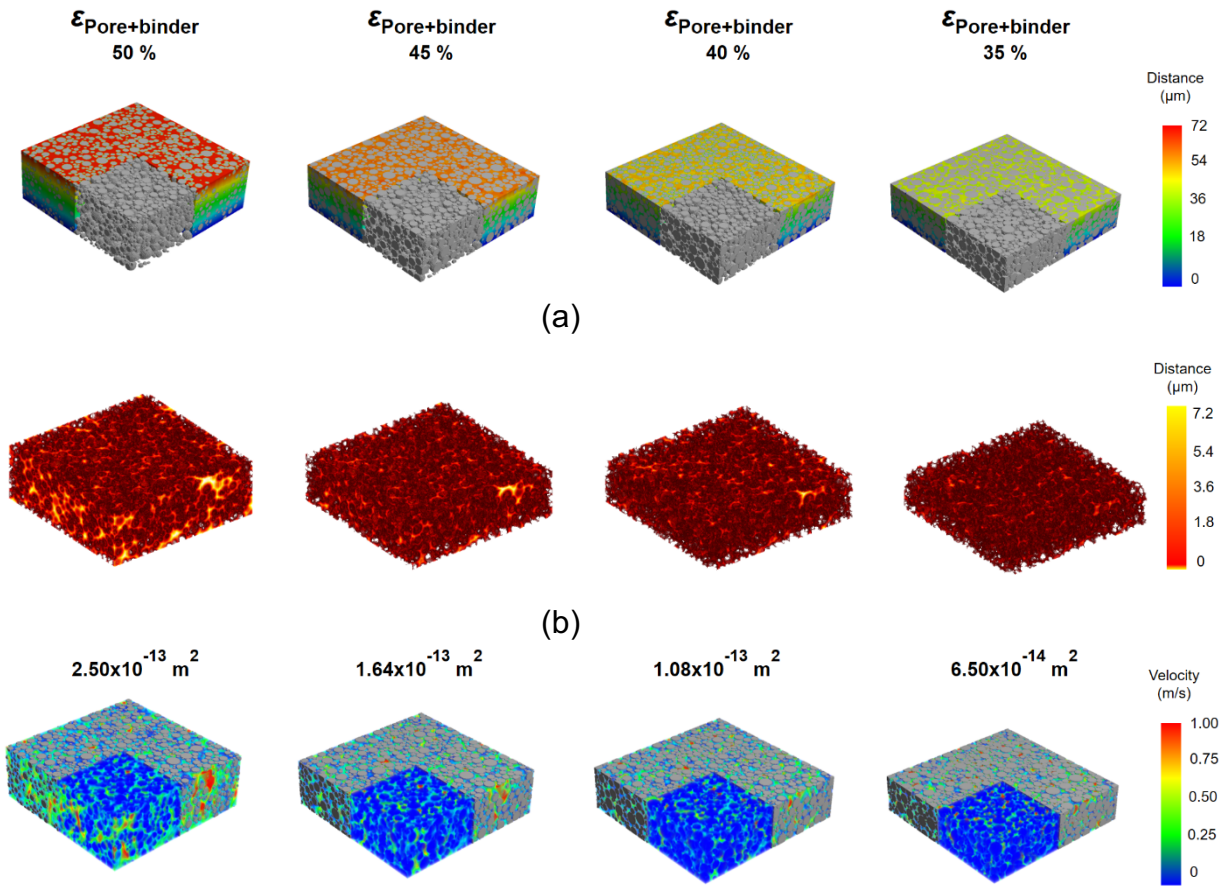

Figure 6 Structure analysis of DEM generated AM particle structures (a) the minimum path length map along z direction (b) inter-particle gap calculated by Euclidean distance transform (c) Flow field calculated by Navier-Strokes equations.

3.2 CBD phase generation and electrochemical analysis

The CBD phase from tomography is further analysed using three-phase-segmentation (Supplementary Figures 1-2). The volume fractions of macro-pore phase for the calendered and uncalendered structures are 11.52 % and 6.19 % respectively. A binder generation algorithm was applied to add an equivalent volume of CBD phase to the corresponding DEM generated structures [18, 30]. It needs to be noted here that the nano-sized pores within the CBD phase are not resolved in the experimental data due to the limited resolution of micro CT, but the macroscopic CBD distribution is. The structures with artificially generated CBD phase were further used in the electrochemical analysis (Supplementary Figure 2), although a smaller subvolume was simulated with a cross-section 80 µm x 80 µm extracted from the original volume. As with the experimental C-rates, the simulations were discharged at a rate of 1C, C/3, C/5, and C/10. The underlying framework for the electrochemical simulations is outlined in the supplementary information (Supplementary Tables 5-8).

In Figure 7 (a) we compare, in a qualitative manner, the state of lithiation and overpotential profiles for an uncalendered tomography-based microstructure and its equivalent idealised case used in DEM. Broadly speaking, we observe very good alignment between the tomography and the idealised versions. However, there are

some minor differences, see for example in Figure 7 (a), where the non-spherical nature of the particle is not observed and it therefore fails to capture the level of heterogeneity that is introduced as a result. Figure 7 (b) shows the state of lithiation profile across the electrode thickness and it's clear that minor differences aside, the same trends in lithiation gradients are observed in both cases. This is further strengthened by the cell voltage response in Figure 7 (c), where the specific capacity of the idealised case is within 0.35% of the tomography-based capacity. It is thus clear that an idealised geometry is sufficient to capture the overall performance of an electrode microstructure.

Figure 8 (a) illustrates the discharge curves for uncalendered and calendered electrodes at a C/3 discharge rate, where decent alignment between experiment and idealised DEM electrochemical model has been achieved. In this first instance we observe an increase in capacity when an electrode has been calendered. Figure 8 (b) shows that the discharge capacity declines with increasing discharge rate. At moderate rates of discharge (C/10 and C/5) the difference in capacity between uncalendered and calendered structures is minimal, however beginning at C/3, we begin to see a significant difference, which is observed both experimentally and numerically. This behaviour can be traced to the electrode microstructure.

Within the present work, this corresponds with electrodes that have an uncalendered thickness of 71 μm and 11.52% porosity, and a calendered thickness of 49 μm thick and 6.19% porosity, with a constant average particle diameter between samples. As illustrated in Figure 8, at a 1C discharge rate for the calendered electrode, we note that the performance, in general, is poor relative to some studies in the literature [31, 32] However, these studies use different formulations (80:10:10) when compared to the 96:2:2 mass ratio here. It is thus likely that the electrodes used here have lower porosity and suffer from lithium-ion transport limitations in general. Consider the state of lithiation profiles across the electrode thickness (at 50% degree of discharge) in Figure 8 (c) and (d), for C/3 and 1C respectively: we observe minor gradients across the electrode thickness at C/3, which indicates that the performance is not restricted by slow lithium ion transport at low rates. Conversely, in the 1C case there is a significant difference between the particle utilisation at the current collector and the separator, reducing the specific capacity. Furthermore, we note that at 1C for the uncalendered electrode (Figure 8 (d)), there is a wide variation in AM utilisation across the electrode, which reinforces the conclusion that electrode thickness plays a role in diminishing the performance of the electrode, despite the increased porosity. We also note that there is a significant difference in voltage plateau (Figure 8 (a)) between the two structures, where the calendered electrode exhibits an elevated voltage profile. We attribute this to the lower overpotentials that occur due to the thinner electrode, which has better transport properties. It is thus clear that calendering improves the electrode performance in this case, however caution must be exercised since particle size and porosity can become a factor; this is discussed in further detail by Lu et al [13].

Finally, we consider a scenario that is critical to the development of next-generation battery electrodes: high rate charging and discharging under cycling conditions. This was carried out at a rate of 5C, for 5 cycles - note that due to computational expense,

no further cycling was simulated. The discharge capacity at 5C is plotted in Figure 9 (a) and indicates that, regardless of the calendering condition, discharge capacity drops significantly at high rate, which we can attribute to the large polarisation experienced at the end of discharging and charging as shown in Figure 9 (b). In the current work we focus on comparisons between calendered and uncalendered electrode microstructures, however detailed discussions on the underlying mechanisms of this high-rate cycling capacity loss can be found in Boyce et al. [33], and Ovejas and Cuadras [34]. It is clear that the calendered electrode performs marginally better, and displays improved material utilisation, shown in the state of lithiation profiles in Figure 9 (c) and (d). Despite the large state of lithiation gradients throughout the electrode, it is evident that the calendered electrode exhibits more homogenous material utilisation relative to that of the uncalendered case after 5 cycles. This has a minor influence on the performance, as described, but does show that calendering makes a difference as a cell is cycled, and this provides a pathway for future work in the computational design of electrodes. This high rate cycling study has highlighted the need for electrode microstructure design in order to improve battery performance, particularly where thick electrodes are concerned. The numerical modelling framework demonstrated here will serve as a powerful microstructure design tool under a wide variety of calendering and operating conditions.

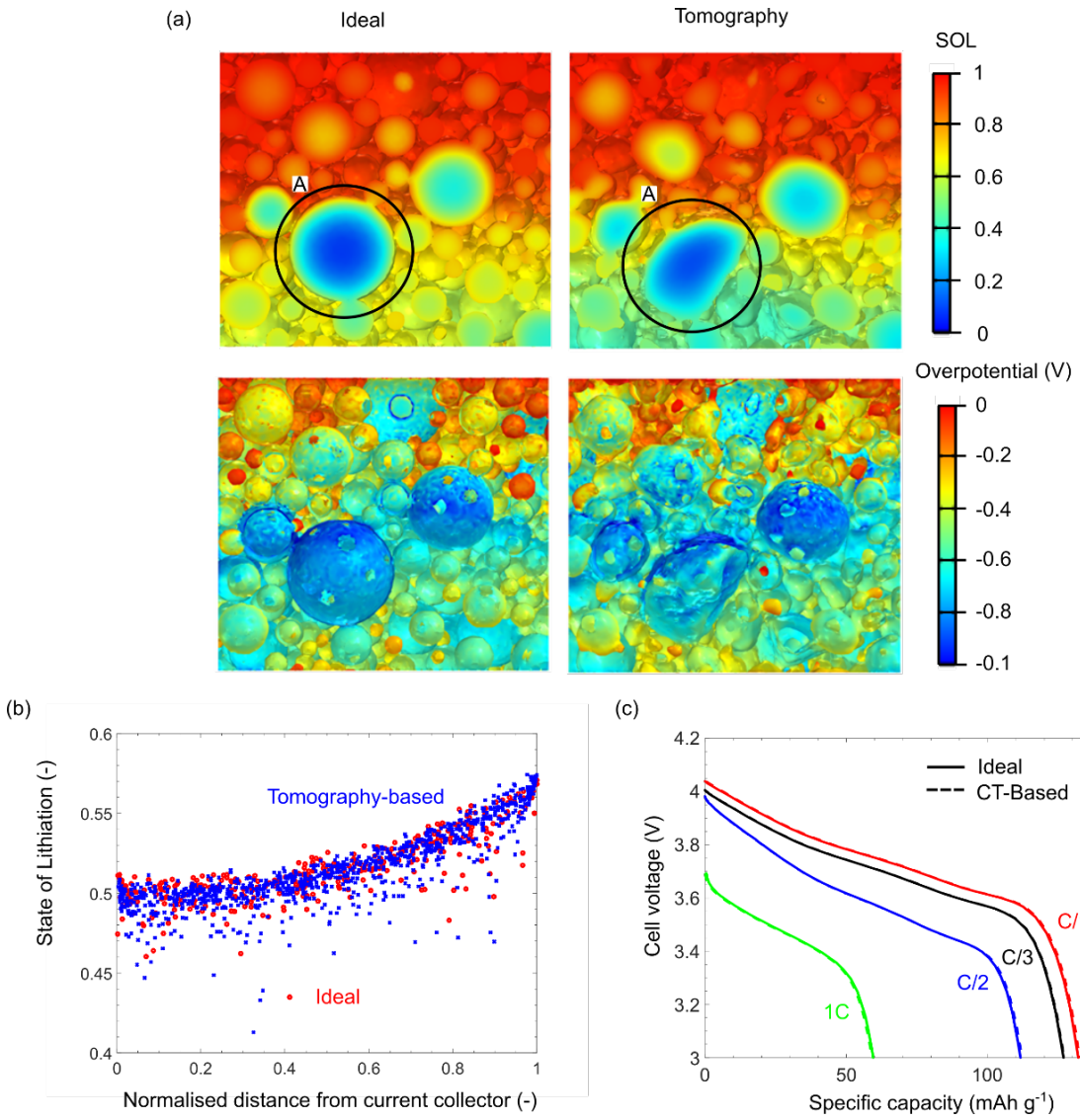

Figure 7. Comparison of (a) the state of lithiation (SOL) and overpotential contours (b) the SOL at the centre point of each particle at 25% degree of discharge and (c) the discharge curve for the tomography-based, and idealised microstructures at different discharge rates.

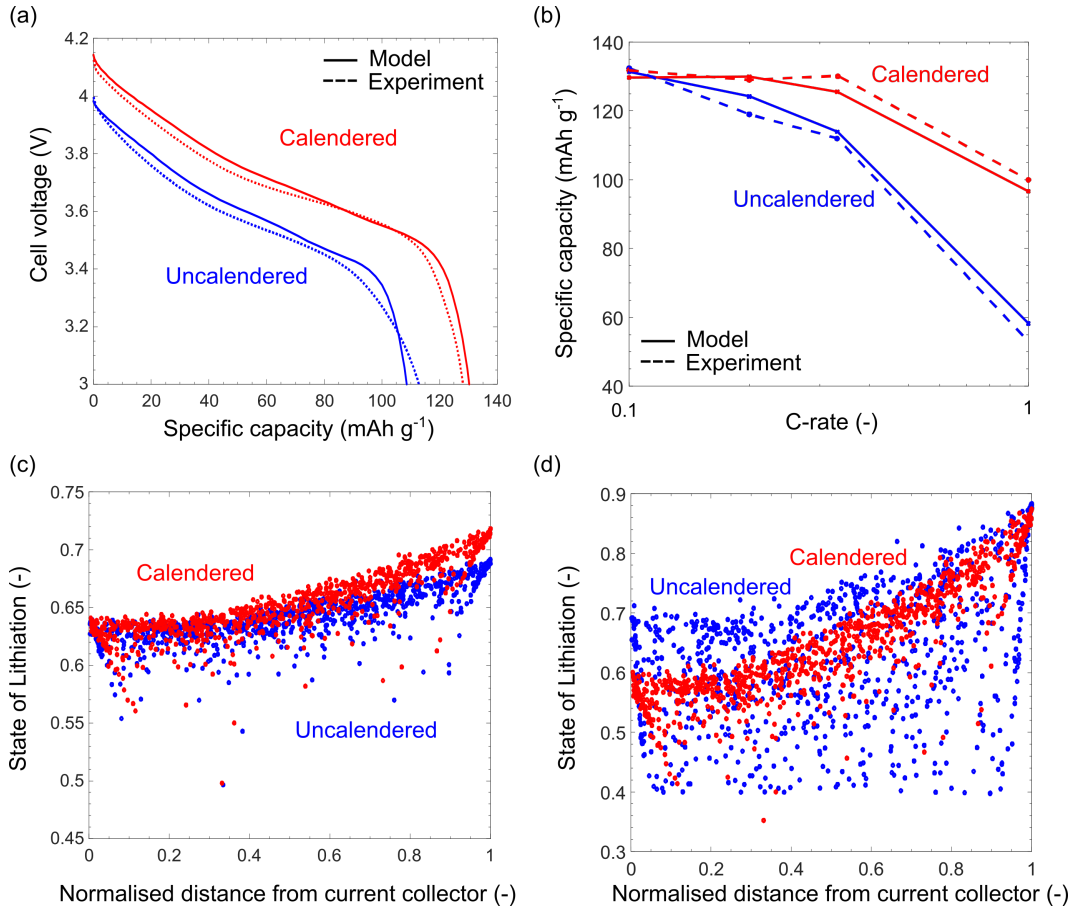

Figure 8. Comparison of (a) the experimental and model voltage response for the uncalendered and calendered electrodes at C/2 discharge rate (b) the specific capacity as a function of discharge rate for model and experiment (c) and (d) the state of lithiation at the centre point of each particle at 50 % degree of discharge for a (c) C/3 and (d) 1C discharge.

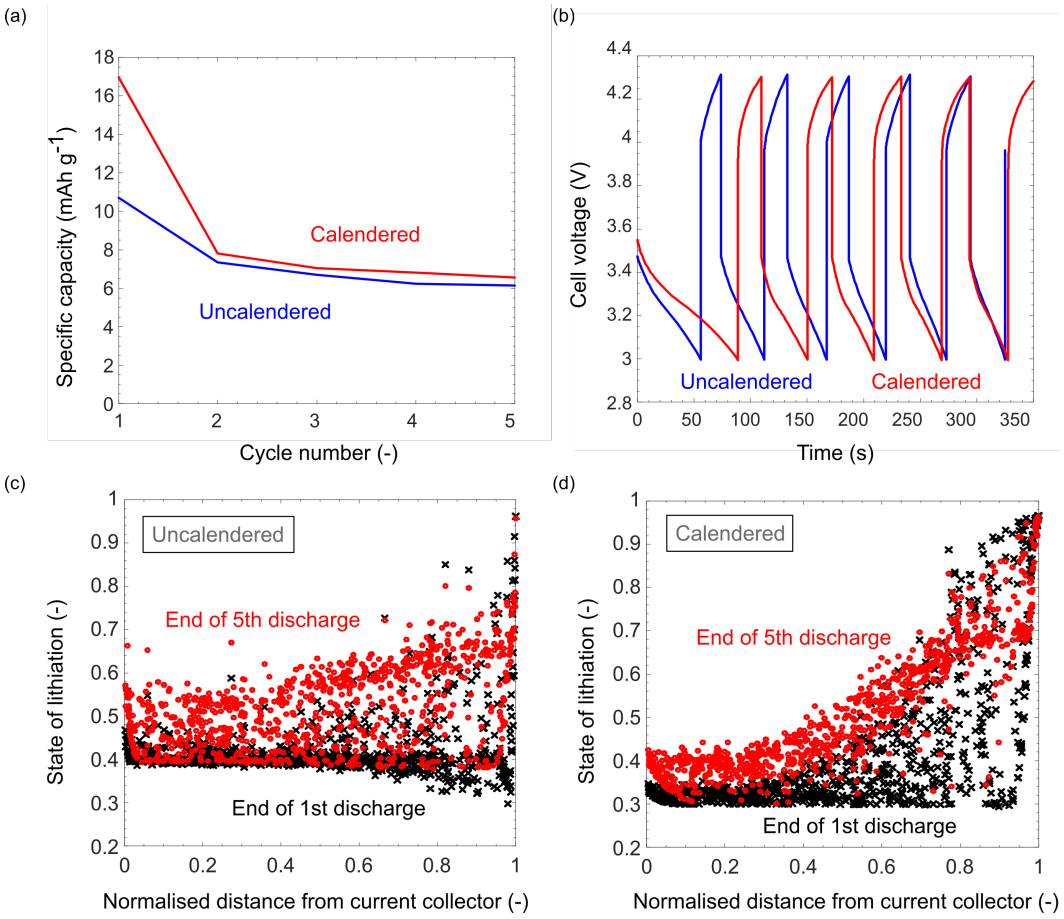

Figure 9. A comparison of uncalendered and calendered electrodes (a) specific discharge capacity as a function of cycle number and (b) cell voltage response versus time. The state of lithiation profiles at the end of the 1st and 5th discharge for uncalendered and calendered electrodes are shown in (c) and (d), respectively.

3.3 Discussion

DEM with a bonded particle model has been demonstrated as a powerful tool to model electrode calendering. Following our previous study [18], a digitalised workflow comprising XCT characterization, DEM, and electrochemical testing is proposed in this work. As illustrated in Figure 10, the digitalised compression process by DEM was benchmarked via corresponding realistic structures from tomography. Good agreement between the physical test and digitalisation of battery design has been achieved. For the AM particle structure without the CBD phase, the porosity distribution, specific surface area and tortuosity were firstly evaluated (Figures 4-5). The battery performance after considering the CBD phase was analysed by electrochemical modelling (Figures 7-9).

The calendering process is highly complex and computationally demanding from a numerical modelling perspective. Future work will include combined features such as rolling press speed, temperature and pressure. With a rigorous validation, the high fidelity DEM simulations can predict microstructure variation, particle scale information and corresponding battery performance under different calendering conditions.

Spherical NMC particles were considered in this model as they are widely used active materials in lithium-ion battery cathodes, however the technique is applicable to non-spherical particles with highly irregular shapes, e.g. single crystal AM particles, using the multi-sphere approach or other advanced shape description algorithms [35, 36], This forms part of our ongoing work.

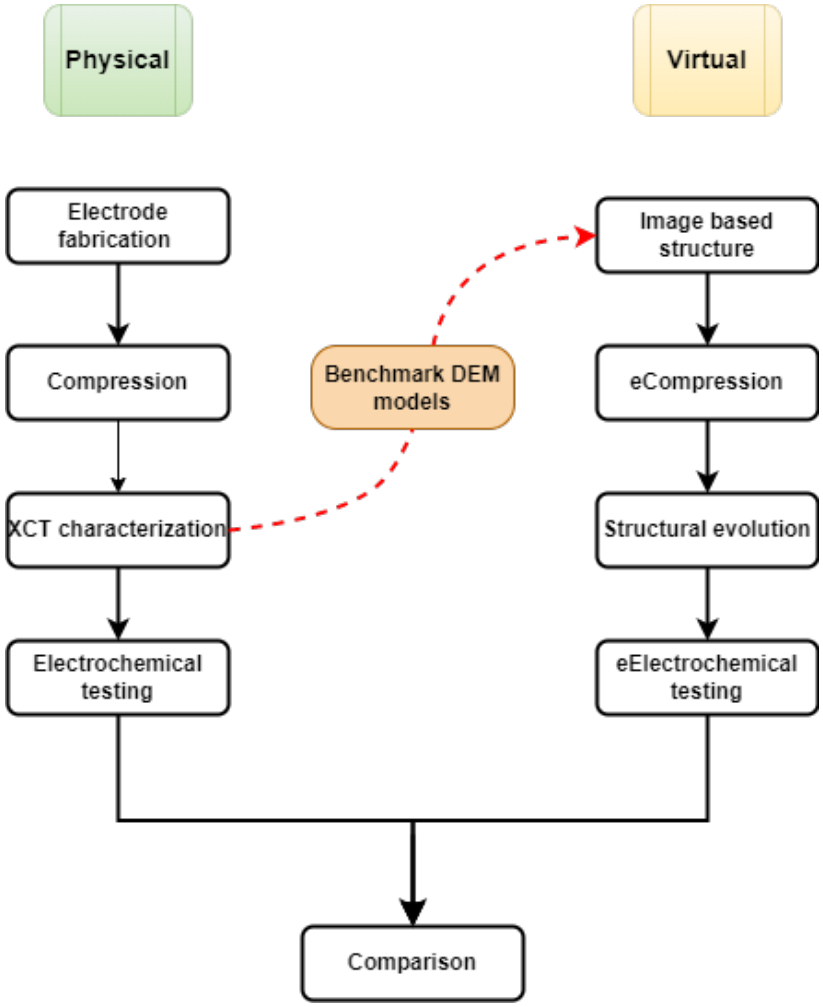

Figure 10. Flow chart of the proposed approach to digitalise the lithium-ion cathode structure evolution during calendering.

The electrochemical simulation results in Figures 7-9 indicate that the microstructure of a lithium ion battery holds significant influence over its performance; the porosity provides a tortuous path for electrolyte percolation and lithium ion transport, the particle size dictates the rate at which lithiation occurs, while the level of carbon binder influences the electronic conduction. These three mechanisms compete in a complex manner and govern the electrode performance. If electrode thickness is increased, then the diffusion length increases, and it takes longer for lithium ions to reach the current collector region within the electrode. This is further exacerbated if the porosity is reduced, which increases the tortuosity. At the same time, if the particle size is reduced (in a volume-fraction-preserving manner), then lithium diffuses more rapidly within the particles, allowing increased particle utilisation [13]. The rate performance

of the electrode is primarily dictated by these mechanisms and a complex multi-parameter optimisation is required. When we calender an electrode we transform the microstructure from a thick, porous state, to a thinner, more densified structure. This implies that we are observing the competition between thickness and porosity and it is clear that, despite the much reduced porosity in the calendered electrode, that the reduction in thickness improves the electrode performance, particularly at 1C (Figure 8).

Electrode optimisation can be achieved via techniques such as grading of pore distributions throughout the electrode that addresses the previously discussed performance limiting mechanisms [37, 38]. These electrode engineering techniques produce complex microstructures, and the combination of XCT and electrochemical simulations permits a greater understanding of the electrode morphology and its influence on battery performance. Furthermore, practical implementation of these electrodes requires calendering and it is important to gain insight into the influence of this process on final electrode performance. The present work has outlined a powerful workflow that combines XCT image-based DEM, and finite element simulations that will serve as the foundation for electrode microstructure optimisation process, enabling the design of superior lithium-ion batteries.

4. Conclusions

In this work, a physics-based modelling approach, i.e. DEM with a bonded particle model, was used to model the lithium ion cathode structure evolutions during calendering. The performance of idealised DEM structures was precisely compared with the realistic structures from tomography and corresponding electrochemical characterisation results. For the first time, a battery performance evaluation and comparison between DEM simulation with complementary electrochemical modelling and tomographic and experimental electrochemical characterisation has been made.

By using the idealised DEM generated structures, a good agreement with the experimental characterisation results can be achieved, demonstrating the idealised structures from DEM can be used for the battery performance evaluation. Electrochemical analysis was performed incorporating CBD phase. The electrochemical analysis further indicates that the thickness reduction after calendering is helpful to improve the battery performance. The porosity distribution, specific surface area and tortuosity of uncalendered/calendered structures were studied. The idealised structures from DEM can capture the porosity distribution and surface area changes. The sphericity and orientation angles of AM particles from tomography scans were analysed. The mean sphericity values are 0.82 and 0.80, and corresponding mean orientation angles are 52.5^{o} and 55.5^{o} for the uncalendered and calendered structures. By well characterised structure properties and experimental comparison, DEM is demonstrated to be useful to model the structural relevant property variations during calendering.

The proposed approach will be further used to investigate the electrode structure evolutions considering different thickness and porosity, providing a valuable tool for electrode design that can be readily adopted.

Acknowledgments

This work was support by Faraday Institution NEXTRODE project (Grant Number: FIRG015). The authors would like to acknowledge Dr. Marina Sousani from Altair EDEM® for advice and discussions about DEM simulations. The support of Altair EDEM® for providing EDEM licences is greatly acknowledged.

References

[1] A. Kwade, W. Haselrieder, R. Leithoff, A. Modlinger, F. Dietrich, K. Droeder, Current status and challenges for automotive battery production technologies, Nature Energy 3(4) (2018) 290-300.
[2] H. Xu, J. Zhu, D.P. Finegan, H. Zhao, X. Lu, W. Li, N. Hoffman, A. Bertei, P. Shearing, M.Z. Bazant, Guiding the Design of Heterogeneous Electrode Microstructures for Li-Ion Batteries: Microscopic Imaging, Predictive Modeling, and Machine Learning, Advanced Energy Materials 11(19) (2021) 2003908.
[3] M. Ebner, F. Geldmacher, F. Marone, M. Stampanoni, V. Wood, X-ray tomography of porous, transition metal oxide based lithium ion battery electrodes, Advanced Energy Materials 3(7) (2013) 845-850.
[4] S.R. Daemi, C. Tan, T. Volkenandt, S.J. Cooper, A. Palacios-Padros, J. Cookson, D.J. Brett, P.R. Shearing, Visualizing the carbon binder phase of battery electrodes in three dimensions, ACS Applied Energy Materials 1(8) (2018) 3702-3710.
[5] L. Zielke, T. Hutzenlaub, D.R. Wheeler, C.W. Chao, I. Manke, A. Hilger, N. Paust, R. Zengerle, S. Thiele, Three-phase multiscale modeling of a LiCoO2 cathode: combining the advantages of FIB–SEM imaging and x-ray tomography, Advanced Energy Materials 5(5) (2015) 1401612.
[6] X. Lu, A. Bertei, D.P. Finegan, C. Tan, S.R. Daemi, J.S. Weaving, K.B. O'Regan, T.M. Heenan, G. Hinds, E. Kendrick, 3D microstructure design of lithium-ion battery electrodes assisted by X-ray nano-computed tomography and modelling, Nature communications 11(1) (2020) 1-13.
[7] L. Zielke, T. Hutzenlaub, D.R. Wheeler, I. Manke, T. Arlt, N. Paust, R. Zengerle, S. Thiele, A combination of x-ray tomography and carbon binder modeling: reconstructing the three phases of LiCoO2 Li-ion battery cathodes, Advanced Energy Materials 4(8) (2014) 1301617.
[8] W. Haselrieder, S. Ivanov, D.K. Christen, H. Bockholt, A. Kwade, Impact of the calendering process on the interfacial structure and the related electrochemical performance of secondary lithium-ion batteries, ECS Transactions 50(26) (2013) 59.
[9] C. Schilcher, C. Meyer, A. Kwade, Structural and electrochemical properties of calendered lithium manganese oxide cathodes, Energy Technology 4(12) (2016) 1604-1610.
[10] E.N. Primo, M. Touzin, A.A. Franco, Calendering of Li (Ni0. 33Mn0. 33Co0. 33) O2-based cathodes: analyzing the link between process parameters and electrode properties by advanced statistics, Batteries & Supercaps 4(5) (2021) 834-844.
[11] R. Sim, S. Lee, W. Li, A. Manthiram, Influence of Calendering on the Electrochemical Performance of LiNi0. 9Mn0. 05Al0. 05O2 Cathodes in Lithium-Ion Cells, ACS Applied Materials & Interfaces 13(36) (2021) 42898-42908.
[12] M. Duquesnoy, T. Lombardo, M. Chouchane, E.N. Primo, A.A. Franco, Data-driven assessment of electrode calendering process by combining experimental results, in silico mesostructures generation and machine learning, Journal of Power Sources 480 (2020) 229103.
[13] X. Lu, S.R. Daemi, A. Bertei, M.D. Kok, K.B. O'Regan, L. Rasha, J. Park, G. Hinds, E. Kendrick, D.J. Brett, Microstructural evolution of battery electrodes during calendering, Joule 4(12) (2020) 2746-2768.
[14] S. Daemi, X. Lu, D. Sykes, J. Behnsen, C. Tan, A. Palacios-Padros, J. Cookson, E. Petrucco, P. Withers, D. Brett, 4D visualisation of in situ nano-compression of Li-ion cathode materials to mimic early stage calendering, Materials Horizons 6(3) (2019) 612-617.

[15] A. Stershic, S. Simunovic, J. Nanda, Modeling the evolution of lithium-ion particle contact distributions using a fabric tensor approach, Journal of Power Sources 297 (2015) 540-550.
[16] R. Ge, M. Ghadiri, T. Bonakdar, Q. Zheng, Z. Zhou, I. Larson, K. Hapgood, Deformation of 3D printed agglomerates: Multiscale experimental tests and DEM simulation, Chemical Engineering Science 217 (2020) 115526.
[17] C.S. Giménez, B. Finke, C. Schilde, L. Froböse, A. Kwade, Numerical simulation of the behavior of lithium-ion battery electrodes during the calendaring process via the discrete element method, Powder Technology 349 (2019) 1-11.
[18] R. Ge, D.J. Cumming, R.M. Smith, Discrete element method (DEM) analysis of lithium ion battery electrode structures from X-ray tomography-the effect of calendering conditions, Powder Technology 403 (2022) 117366.
[19] I. Srivastava, D.S. Bolintineanu, J.B. Lechman, S.A. Roberts, Controlling Binder Adhesion to Impact Electrode Mesostructures and Transport, ACS applied materials & interfaces 12(31) (2020) 34919-34930.
[20] A.C. Ngandjong, T. Lombardo, E.N. Primo, M. Chouchane, A. Shodiev, O. Arcelus, A.A. Franco, Investigating electrode calendering and its impact on electrochemical performance by means of a new discrete element method model: Towards a digital twin of Li-Ion battery manufacturing, Journal of Power Sources 485 (2021) 229320.
[21] Y.S. Zhang, A.N. Pallipurath Radhakrishnan, J.B. Robinson, R.E. Owen, T.G. Tranter, E. Kendrick, P.R. Shearing, D.J. Brett, In Situ Ultrasound Acoustic Measurement of the Lithium-Ion Battery Electrode Drying Process, ACS Applied Materials & Interfaces 13(30) (2021) 36605-36620.
[22] S. Berg, D. Kutra, T. Kroeger, C.N. Straehle, B.X. Kausler, C. Haubold, M. Schiegg, J. Ales, T. Beier, M. Rudy, Ilastik: interactive machine learning for (bio) image analysis, Nature Methods 16(12) (2019) 1226-1232.
[23] B. Münch, P. Gasser, L. Holzer, R. Flatt, FIB‐Nanotomography of Particulate Systems—Part II: Particle Recognition and Effect of Boundary Truncation, Journal of the American Ceramic Society 89(8) (2006) 2586-2595.
[24] S.C. Thakur, J.P. Morrissey, J. Sun, J. Chen, J.Y. Ooi, Micromechanical analysis of cohesive granular materials using the discrete element method with an adhesive elasto-plastic contact model, Granular Matter 16(3) (2014) 383-400.
[25] D.O. Potyondy, P. Cundall, A bonded-particle model for rock, International journal of rock mechanics and mining sciences 41(8) (2004) 1329-1364.
[26] S.J. Cooper, A. Bertei, P.R. Shearing, J. Kilner, N.P. Brandon, TauFactor: An open-source application for calculating tortuosity factors from tomographic data, SoftwareX 5 (2016) 203-210.
[27] H. Wadell, Volume, shape, and roundness of quartz particles, The Journal of Geology 43(3) (1935) 250-280.
[28] B. Münch, L. Holzer, Contradicting geometrical concepts in pore size analysis attained with electron microscopy and mercury intrusion, Journal of the American Ceramic Society 91(12) (2008) 4059-4067.
[29] B.L. Trembacki, D.R. Noble, M.E. Ferraro, S.A. Roberts, Mesoscale effects of composition and calendering in lithium-ion battery composite electrodes, Journal of Electrochemical Energy Conversion and Storage 17(4) (2020) 041001.
[30] A.N. Mistry, K. Smith, P.P. Mukherjee, Secondary-phase stochastics in lithium-ion battery electrodes, ACS applied materials & interfaces 10(7) (2018) 6317-6326.
[31] Y. Chen, S. Tang, S. Deng, T. Lei, Y. Li, W. Li, G. Cao, J. Zhu, J. Zhang, Chemical coupling constructs amorphous silica modified LiNi0. 6Co0. 2Mn0. 2O2 cathode materials and its electrochemical performances, Journal of Power Sources 431 (2019) 8-16.
[32] B. Chu, G. Li, L. You, T. Huang, M. Liu, A. Yu, Enhancing the air stability of LiNi0. 6Co0. 2Mn0. 2O2 cathode through WO3/Li2WO4 surface modification, Journal of Power Sources 514 (2021) 230605.

[33] A.M. Boyce, E. Martínez-Pañeda, A. Wade, Y.S. Zhang, J.J. Bailey, T.M. Heenan, D.J. Brett, P.R. Shearing, Cracking predictions of lithium-ion battery electrodes by X-ray computed tomography and modelling, Journal of Power Sources 526 (2022) 231119.
[34] V. Ovejas, A. Cuadras, Effects of cycling on lithium-ion battery hysteresis and overvoltage, Scientific reports 9(1) (2019) 1-9.
[35] G. Mollon, J. Zhao, 3D generation of realistic granular samples based on random fields theory and Fourier shape descriptors, Computer Methods in Applied Mechanics and Engineering 279 (2014) 46-65.
[36] J.C. Bonaldo, S. Mazerat, S. Romero-Baivier, C.L. Martin, Microstructure-based discrete simulations of the compaction of refractory powder composites, Powder Technology (2022) 117577.
[37] C. Cheng, R. Drummond, S.R. Duncan, P.S. Grant, Micro-scale graded electrodes for improved dynamic and cycling performance of Li-ion batteries, Journal of Power Sources 413 (2019) 59-67.
[38] C. Huang, M. Dontigny, K. Zaghib, P.S. Grant, Low-tortuosity and graded lithium ion battery cathodes by ice templating, Journal of Materials Chemistry A 7(37) (2019) 21421-21431.